Supporting Information for

Electrolyte-resistive dual materials for the synergistic safety enhancement of lithium ion batteries

Lien-Yang Chou, Yusheng Ye, Hiang Kwee Lee, Wenxiao Huang, Rong Xu, Xin Gao, Renjie Chen, Feng Wu, Chia-Kuang Tsung and Yi Cui[*]

[*]Corresponding author. E-mail: yicui@stanford.edu

Materials and Methods

Fabrication of the composite separator

DBDPE (TCI, JP) and PVDF (MTI, CA) powders were dispersed in N-methyl-2-pyrrolidone (NMP, Sigma Aldrich, USA) to prepare a slurry (mass ratio of DBDPE:PVDF is 9:1). The slurry was stirred overnight and then coated on one side of a commercially available 12-μm-thick microporous PE separator membrane (Teklon Gold LP from Entek Membranes, USA) with a doctor blade. The slurry-coated separator was dried in a vacuum oven at 60 °C for 12 h. For the preparation of a composite separator with Sb_2O_3 (Sigma Aldrich, USA), the same reaction parameters were used, except that a mixture of Sb_2O_3 and DBDPE was used. The solid mixture was added with PVDF powder and dispersed in NMP. The mass ratio of the mixture and PVDF was maintained at 9:1.

Characterization methods

SEM images were captured on a FEI XL30 Sirion scanning electron microscope (FEI, USA). To evaluate the mechanical strength of porous composite polymer films, their tensile stress and strain were measured using a micromaterials tester (Instron, USA). Each specimen was trimmed to a width of 15 mm and a length of 150 mm and was then pulled at the rate of 50 mm min^{-1}. Contact angle measurement was performed using a

JC2000C Contact Angle Meter (Zhongchen, China). To evaluate the thermal shrinkage behavior, the separator was placed in an oven and heated at 150 °C for 0.5 h. TGA was performed on a TA Instruments Q500 thermogravimetric analyzer (TA, USA) at a heating rate of 5 °C/min under simulated air atmosphere (20% O_2 + 80% Ar). XPS analysis was performed on an SSI S-Probe XPS spectrometer (SSI, USA) with an Al $K\alpha$ source. The SET was used to quantitatively estimate the flammability of the electrolytes (1.0 M $LiPF_6$ in 1:1 (v/v) EC/DEC; BASF, Germany). It was obtained by igniting the small specimens of separators (6 cm^2) soaked in the electrolyte (~75 mg). After they were ignited by exposing to a direct flame, the time for the flame to self-extinguish was recorded and then normalized by the electrolyte mass. For testing the SET of a pouch cell (85 mAh), graphite (MTI, CA) and LCO (MTI, CA) were used as the anode and cathode, respectively. Approximately 750 mg of the electrolyte was soaked in the pouch cell and used for normalized SET measurements.

Electrochemical testing

Coin cells (2032-type, MTI, CA) were used for electrochemical testing. Battery cycling data were collected using LAND eight-channel battery testers (LAND, China) at room temperature (~24 °C). The LCO electrode was used as the cathode. Lithium foil (Alfa Aesar, USA) was used as the anode. The PE separator and composite separators were

soaked in the electrolyte (1.0 M $LiPF_6$ in 1:1 (v/v) EC/DEC) without other additives. The coating layer on the separator faced the cathode. The capacities and Coulombic efficiencies of the lithium stripping/plating processes were evaluated through galvanostatic cycling of the coin cells. To prepare the LCO electrodes, the LCO powder (MTI, CA), carbon black (TIMCAL, Swiss), and PVDF were mixed in an 8:1:1 ratio with NMP as the solvent. Next, the slurry was cast on an alumina foil, dried at room temperature, and punched into 1-cm^2 electrodes. To ensure that the electrodes were fully dried, they were heated in a vacuum oven at 100 °C for 4–5 h and then stored in an argon-filled glove box for one day. EIS was also carried out on a VMP3 system (BioLogic, French) on symmetric coin cells with ac oscillation amplitude of 10 mV in the frequency range from 100 kHz to 100 Hz. Symmetric coin cells were constructed with stainless steel (MTI, CA) on both sides of the separators using 1.0 M $LiPF_6$ in 1:1 (v/v) EC/DEC as the electrolyte. CV was carried out on a VMP3 system using asymmetric coin cells. Asymmetric coin cells were prepared using lithium foil on one side and stainless steel on the other side of the separator. The coating layer on the separator faced the stainless-steel part of the cell. CV curves were recorded in the voltage range of 4.2 to 0 V versus Li/Li^+ at a scan rate of 1.0 mV/s using 1.0 M $LiPF_6$ in 1:1 (v/v) EC/DEC as the electrolyte.

Nail penetration

Pouch cells (2 Ah) of dimensions 85 mm × 40 mm × 5 mm were assembled with graphite as the anode and LCO as the cathode. The pouch cell was soaked in the electrolyte (1.0 M $LiPF_6$ in 1:1 (v/v) EC/DEC, 6 g) and penetrated by nails, and the internal temperature and voltage of the cells were monitored simultaneously. The internal shorting of the batteries caused by nail penetration was simulated using the electrochemical–thermal coupled model in COMSOL Mutiphysics 5.3, Sweden. The electrochemical model simulated the short-circuit-induced self-discharge of the active materials and the increase in the local temperature of the batteries caused by the shorting current. The local temperature increase via Joule heating was simulated by the heat transfer model in which the time-dependent temperature distribution in batteries was solved simultaneously with the electrochemical self-discharge. To simplify, we modeled a single layer of the battery consisting of a graphite anode and a $LiCoO_2$ cathode with the electrolyte of 1 M $LiPF_6$ in EC:DEC solvent (5:5 v/v). The electrochemical properties of the cathode, anode, and electrolyte were adopted from the COMSOL Materials Library. The thermal properties of all the components in batteries and other parameters used in the simulation are listed in Supplementary Table 1. The cell is represented in an axisymmetric geometry with a radius of 14 mm. The initial cell voltage is 4.2 V and the anode side is grounded. The penetration of a stainless-steel nail

through the center of the cell caused an internal short circuit. To model the internal

shorting, the conductivity of the nail was initially set to be low and then increased to a

high value in a short time (1 s) after the nail penetration. To simulate the protective

function of the fire-retardant coating, we assumed that a nonconductive layer gradually

formed on the surface of the stainless-steel nail after the local temperature of the

separator reached 130 °C. The thickness of the nonconductive layer was set as 10 μm

and the forming time was set as 20 s.

a

b

$$Br\bullet + H\bullet \longrightarrow HBr$$

$$HBr + H\bullet \longrightarrow H_2 + Br\bullet$$

$$HBr + OH\bullet \longrightarrow H_2O + Br\bullet$$

c

$$Sb_2O_3 + 6HBr \longrightarrow 2SbBr_3 + 3H_2O$$
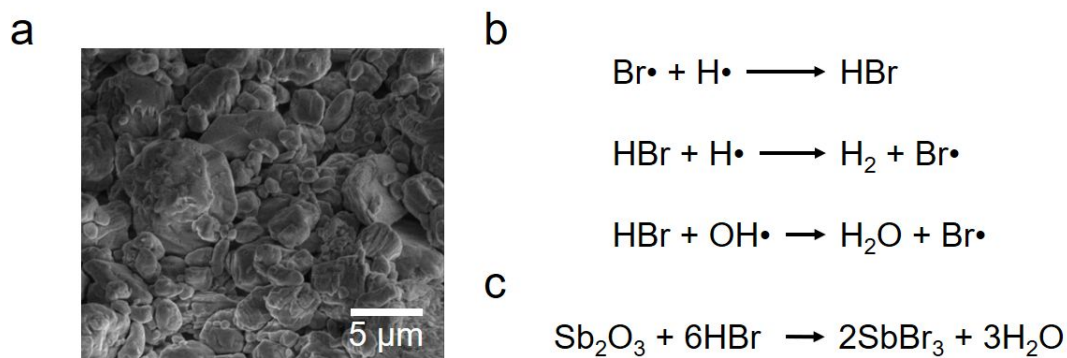
Figure S1. The morphology and flame-retardancy mechanism of DBDPE. (a) SEM image of DBDPE and (b) a radical scavenging mechanism of bromine radicals to neutralize H• and HO• radicals emitted by the chain reaction of the burning electrolyte. (c) Synergism of DBDPE and Sb_2O_3 occur to generate Sb_2Br_3. Here, HBr is produced resulting from the decomposition of DBDPE and electrolyte.
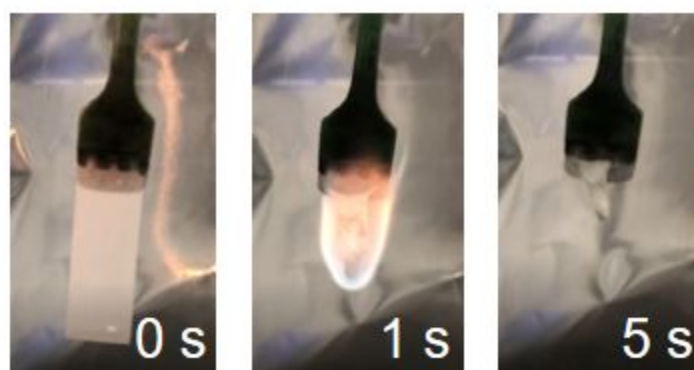
Figure S2. Burning of FR coated separators. Photographs recording the burning of 11 μm DBDPE coated separator.

a			b

a

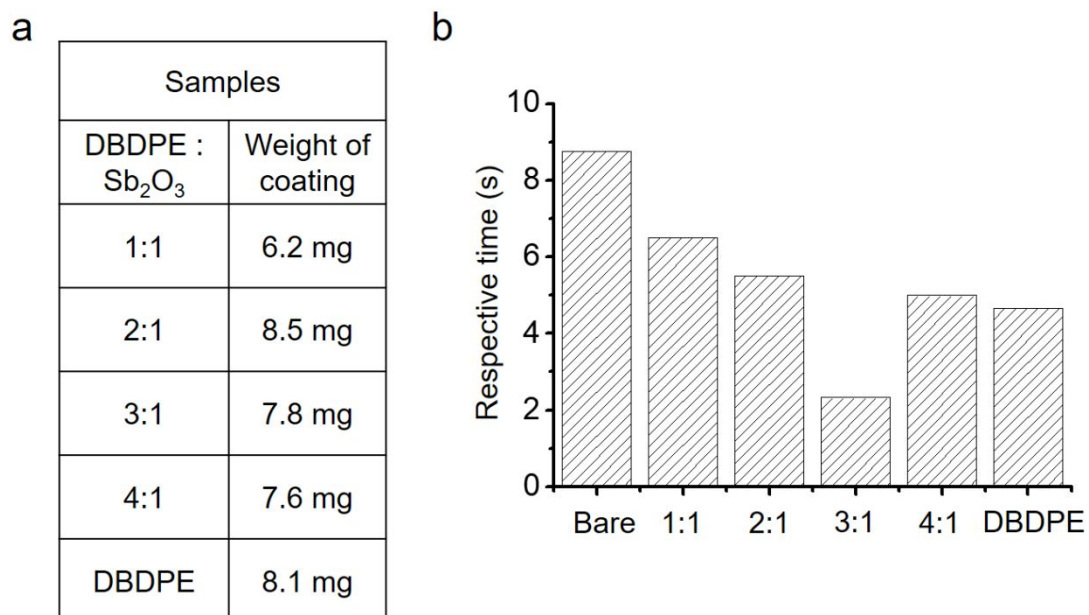| Samples	
DBDPE : Sb_2O_3	Weight of coating
1:1	6.2 mg
2:1	8.5 mg
3:1	7.8 mg
4:1	7.6 mg
DBDPE	8.1 mg

b

Figure S3. The flame retardancy of different ratio of DBDPE and Sb_2O_3 additive. (a) Controlled similar coating weight with different ratio of DBDPE and antimony trioxide. (b) the flame retardancy of the samples above.
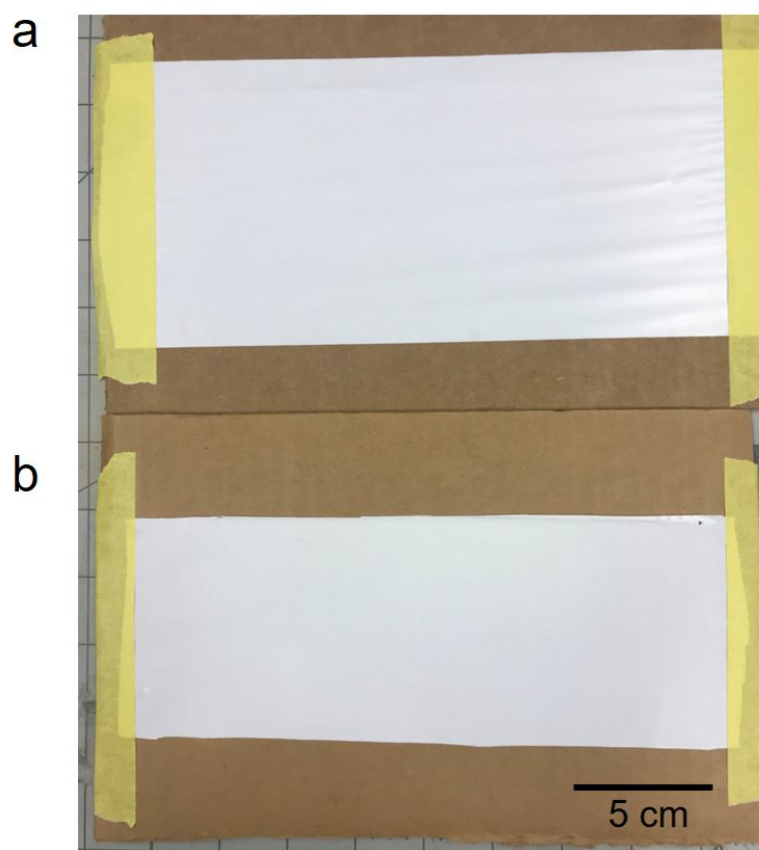
Figure S4. Photographs of bare PE and as-fabricated dual FR composite separator. (a) Bare PE and (b) as-fabricated dual FR composite separator.
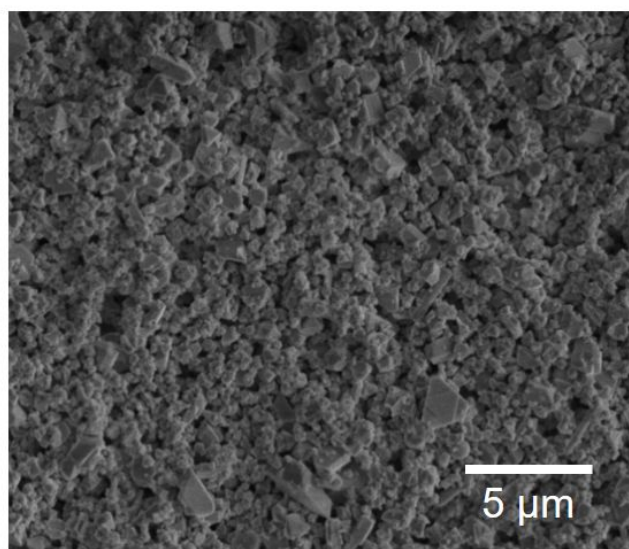
Figure S5. The morphology of Sb_2O_3. SEM image of antimony trioxide.
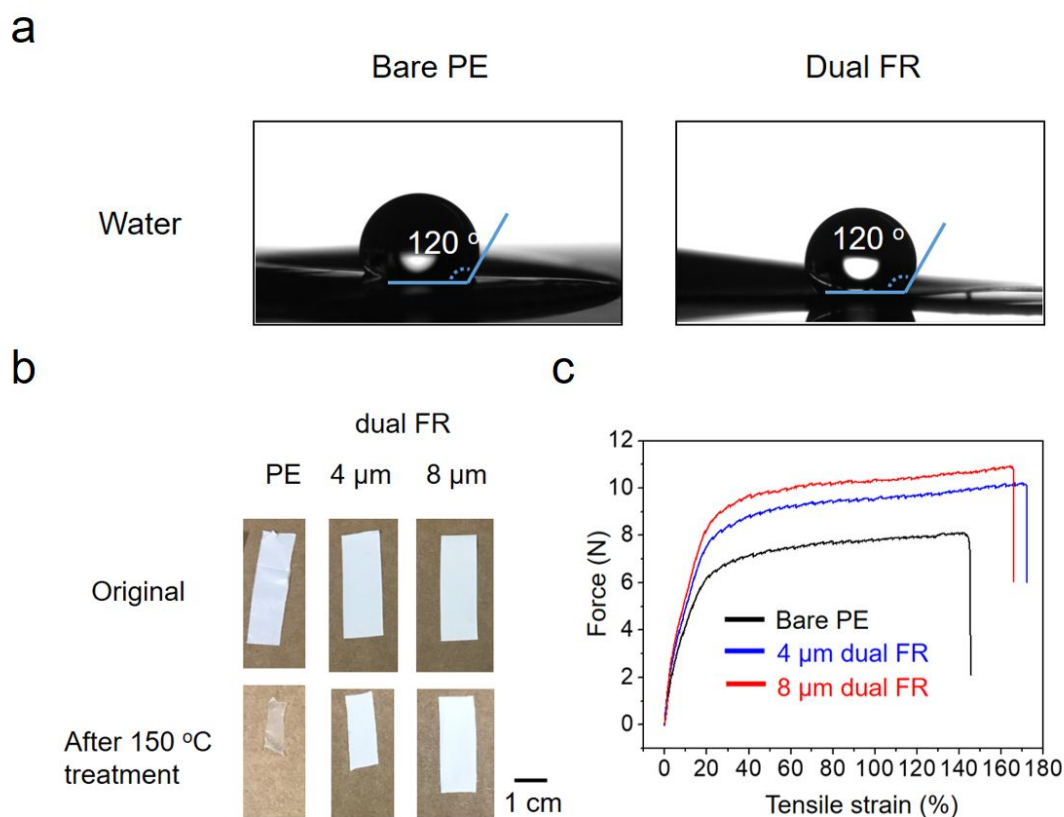
Figure S6. The characterizations of dual FR composite separators. (a) Contact angle images of water on bare PE and dual FR composite separators. (b) Photographs of thermal stability of bare PE and dual FR composite separators. Thermal treatment on bare PE and 4 μm and 8 μm dual FR composite separators at 150 °C for 30 minutes. Original samples were cut to 3 cm x 1 cm (upper) and the shrinkage of samples was measured after heat treatment (lower). (c) Mechanical strength of total force versus tensile strain plot on bare PE and dual FR composite separators.
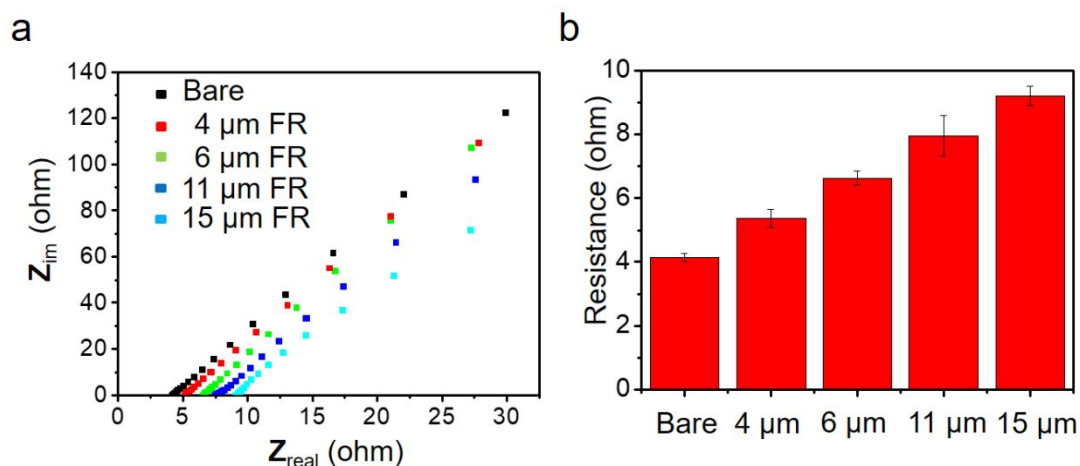
Figure S7. The resistances of DBDPE composite separators. (a) Nyquist plots obtained by EIS, and (b) The resistances of composite separators with different thickness of DBDPE coating layers. The values are calculated as the intercept of the impedance curve to the x-axis. The error bars represent the average deviation.
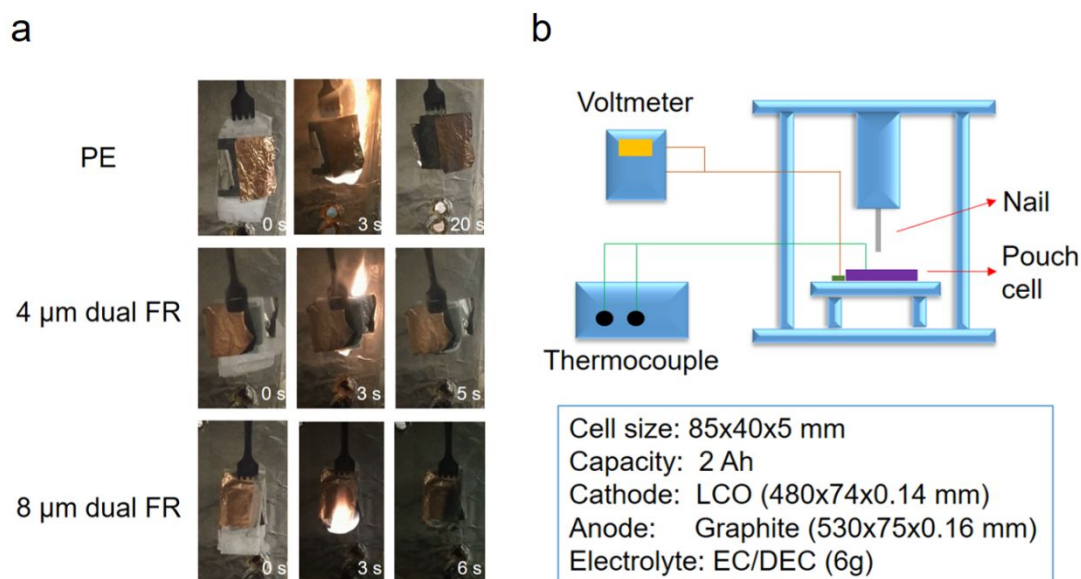

Figure S8. Burning and nail penetration test on full pouch cells. (a) Photographs recording the burning of pouch cells with bare PE separator, 4 μm and 8 μm dual FR composite separators. (b) A schematic illustration of the nail penetration test. 2 Ah pouch cells were assembled with Graphite/ separator + EC/DEC/ LCO and penetrated by nails while the internal temperature and voltage of the cells were monitored.
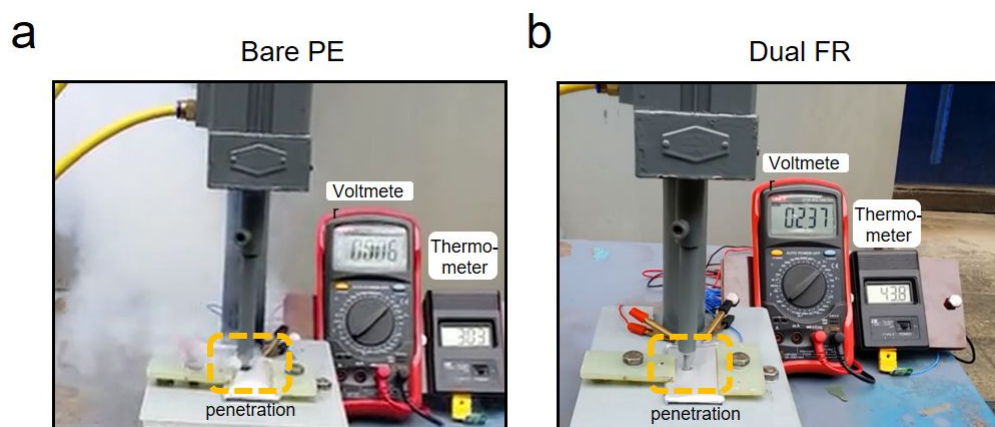
Figure S9. Photographs of nail penetration of pouch cells. Photographs of nail penetration of pouch cells with (a) bare PE separator, and (b) dual FR composite separator.
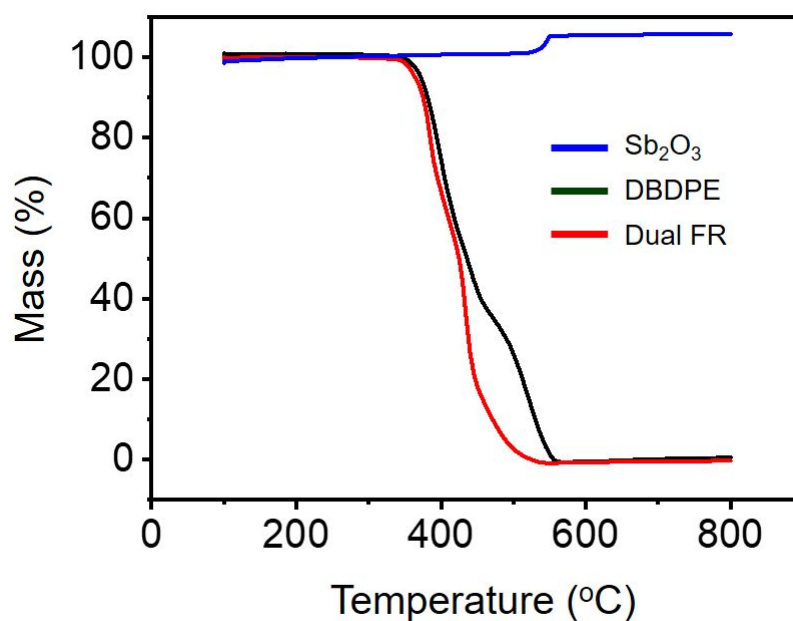

Figure S10. TGA **analysis** of dual FR. TGA analysis of DBDPE (black), antimony trioxide (blue) and dual FR (Red).
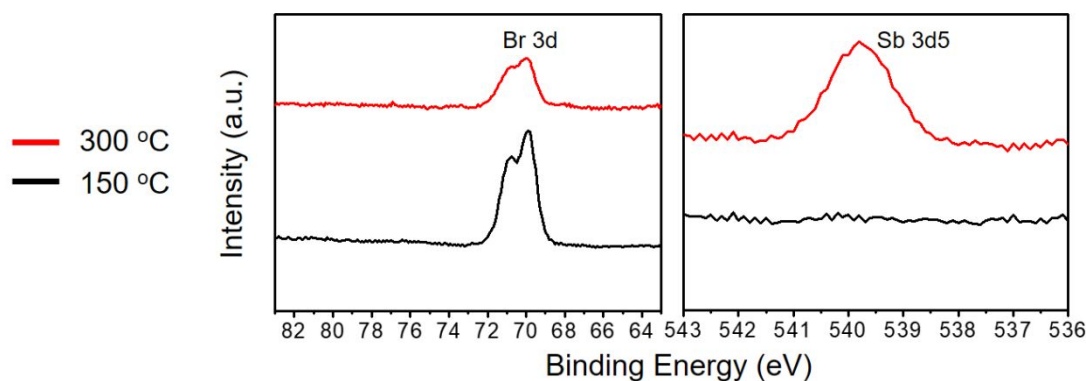
Figure S11. XPS spectra after thermal decomposition of dual FR over 150 °C. **Layer formation from thermal treated dual FR (150-300 °C).** XPS spectra was measured for bromine and antimony on the surface of stainless steel after thermal decomposition of dual FR with different temperatures.

COMSOL simulation:

To further understand the effects of the passive surface layer formation on nail shorting, we performed a COMSOL simulation of the battery behavior upon nail penetration using the electrochemical–thermal coupled model in COMSOL Multiphysics 5.3 (Figure S12a). The electrochemical model simulated the short-circuit-induced self-discharge of the active materials and the increase in the local battery temperature caused by the shorting current. The local temperature increase from Joule heating was simulated by the heat transfer model, in which the time-dependent temperature distribution in the batteries was solved simultaneously with the electrochemical self-discharge (Figure S12b). To simulate the protective function of the dual FR coating, we assumed that a nonconductive layer gradually formed on the surface of the stainless-steel nail after the local temperature of the separator reached 130 °C based on the XPS analyses (Table S1). The thickness of the nonconductive layer was set to 10 μm, and the forming time was set to 20 s.

The simulated cell voltage evolution after nail penetration was similar to the experimental results (Figure S12c). After penetration occurs, the cell voltage quickly drops due to internal shorting. The shorting current passing through the nail generates Joule heat, which increases the local temperature. Without the inductive layer formed by the dual FR, the local temperature can easily increase and further cause the electrolyte and separator to decompose. However, with the dual FR coating, the increase in local temperature leads to the decomposition of DBDPE, forming a nonconductive layer on the surface of the stainless-steel nail that serves as a barrier

between the nail and cell. As the internal short circuit is cut off by the insulating layer, the cell voltage recovers and gradually reaches a steady state that is slightly lower than the initial state due to the partial self-discharge that occurred during the internal short. More importantly, the local temperature near the stainless-steel nail cannot increase indefinitely, as shown in Figure S12d. Instead, the local temperature reaches approximately 70 °C upon shorting before the nonconductive layer automatically shuts down the short. This agrees with the temperature profiles from the experimental nail penetration tests.
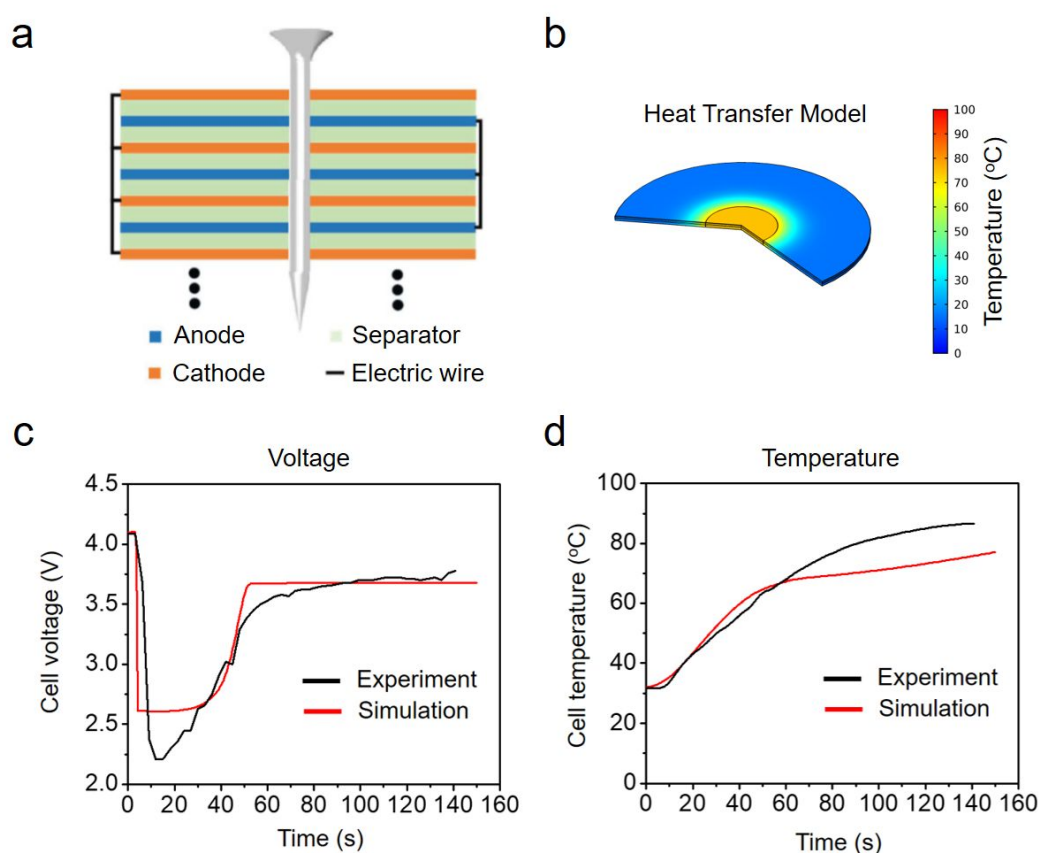

Figure S12. Simulation of the internal short by a nail penetration test. (a) Electrochemical–thermal coupled model in COMSOL. (b) Heat transfer model for simulating the local temperature. Simulated cell (c) voltage and (d) temperature after nail penetration

Table S1. Parameters used in the nail penetration simulation.

Material	Thickness	Density	Electrical	Thermal	Heat

	(μm)	(kg/m^3)	conductivity (S/m)	conductivity (W/(m·K))	capacity (J/(kg·K))
LiCoO$_2$ cathode	40	2500	*N/A*	0.3	1000
Graphite anode	60	2270	*N/A*	0.1	881
Separator	30	940	1×10^{-10}	0.15	1046
Stainless-steel nail	136	7700	1×10^{6}	15	502
Nonconductive layer	10	1000	5×10^{-5}	1	1000